Research Square

Preprints are preliminary reports that have not undergone peer review.
They should not be considered conclusive, used to inform clinical practice,
or referenced by the media as validated information.

Anisotropy in Phonon Thermal Conductivity Reduction of Binary Zr-1%Nb Alloy: Atomistic Simulations of Point Defect Scattering

Mohamad Rajabi
Isfahan University of Technology
Maryam Hassanvand
Isfahan University of Technology
Mohsen Asadi Asadabad
msasadi@aeoi.org.ir

Nuclear Science and Technology Research Institute
mohamad Amin Amirkhani
Nuclear Science and Technology Research Institute

Research Article

Keywords: Phonon Thermal Conductivity (κph), Point Defect, Müller-Plathe, Zr-1%Nb, Direct Thermostat, Green-Kubo

Posted Date: June 18th, 2026

DOI: https://doi.org/10.21203/rs.3.rs-9871857/v1

License: This work is licensed under a Creative Commons Attribution 4.0 International License.
Read Full License

Additional Declarations: No competing interests reported.

Version of Record: A version of this preprint was published at Applied Physics A on August 14th, 2026.
See the published version at https://doi.org/10.1007/s00339-026-09985-2.

Anisotropy in Phonon Thermal Conductivity Reduction of Binary Zr-1%Nb Alloy: Atomistic Simulations of Point Defect Scattering

M. Rajabi[1], M. Hassanvand[1], M. Asadi Asadabad[2*], M. A. Amirkhani[2]

[1] Department of physics, Isfahan University of Technology, 84156-83111, Isfahan, Iran

[2] Reactor and Nuclear Safety Research School, Nuclear Science and Technology Research Institute, Tehran, Iran

Abstract

The thermal conductivity (κ) of the Zr-1%Nb alloy is crucial for the optimal and safe performance of VVER reactors. This paper first provides a comparative analysis of three molecular dynamics methods: Non-Equilibrium Molecular Dynamics (NEMD) and the Equilibrium method (EMD). Within NEMD, two approaches are discussed: the Direct Thermostat Method, which enforces a temperature gradient between two regions and measures the heat flux, and the Müller-Plathe Method, which creates a small temperature gradient by swapping the kinetic energy of atoms between two defined regions and then measuring the exchanged energy. The EMD method, based on the Green-Kubo formalism, utilizes the heat flux autocorrelation function to calculate κ. The results indicate that while the Green-Kubo method requires smaller simulation boxes and is less influenced by size and statistical sample effects, it exhibits lower accuracy due to the exclusion of three-body potential contributions. The Direct Thermostat Method necessitates a large temperature gradient to achieve accurate heat flux measurements, which can distort the results. In terms of total simulation time and accuracy, the Müller-Plathe Method is more suitable for studying irradiated Zr-1%Nb alloys. Results also show centerline temperature variations due to different phonon thermal conductivity (κ_{ph}) methods remain below 0.05°C, demonstrating that phonon modeling uncertainties negligibly affect steady-state fuel thermal performance. This study then employs the Müller-Plathe method to investigate the impact of anisotropic distribution of point defects on the κ_{ph} in Zr-1%Nb alloy. The findings reveal that vacancy defects have a greater impact on reducing κ_{ph}. Additionally, the reduction in κ_{ph} varies among different defects in different directions, which can be attributed to their anisotropic distribution. It is important to note that only the phonon contribution is considered in this study.

Keywords: Phonon Thermal Conductivity (κ_{ph}), Point Defect, Müller-Plathe, Zr-1%Nb, Direct Thermostat, Green-Kubo

* *Corresponding Author name*: M. Asadi Asadabad
E-mail address: msasadi@aeoi.org.ir

1. Introduction

Nuclear energy plays a pivotal role in providing a reliable, low-carbon source of electricity, making it a critical component of the global energy portfolio. One of the key materials used in nuclear reactors is fuel cladding, which acts as a barrier between the nuclear fuel and the reactor coolant, ensuring safety and efficiency of heat transfer [1]. Zirconium-based materials are commonly used for cladding due to their excellent mechanical and thermal properties, low thermal neutron absorption cross-section, and high corrosion resistance [2-5]. Adding a small amount of niobium to zirconium enhances its corrosion resistance and mechanical properties [6, 7]. However, because niobium is present in low concentrations, the alloy properties remain similar to pure zirconium, including a hexagonal close-packed (HCP) structure at low temperatures. At high pressures, the distribution of niobium remains largely homogeneous [8].

Nuclear fuel cladding operates under extreme conditions such as high temperature and pressure, aggressive corrosion environments, and various forms of irradiation resulting from nuclear fuel fission. A significant aspect of irradiation damage caused by high-energy neutrons is displacement damage, where atoms are displaced from their crystal lattice positions [9, 10]. This damage leads to the formation of point defects, displacement cascades, and dislocation loops, resulting in larger structural defects like swelling, cracking, embrittlement, growth, and creep, which significantly affect the performance, lifetime, and safety of the cladding [11-15]. Understanding the thermal properties of this alloy is essential for optimizing reactor performance and ensuring operational safety [16]. Thermal conductivity (κ) is a critical physical property influencing heat transfer in nuclear fuel cladding, directly affecting reactor safety and efficiency [17-20]. This property is influenced by the material's atomic and molecular structure, alloy composition, crystal defects, impurities, and factors such as temperature and pressure. In zirconium-based alloys, κ is intrinsically anisotropic due to their HCP crystal structure. This anisotropy leads to direction-dependent heat transport, with thermal conductivity along the basal and prismatic directions differing significantly. Such directional variation can alter the local temperature gradients in the cladding under operational conditions, thereby influencing dimensional stability, stress evolution, and defect dynamics during irradiation. Consequently, accurate evaluation of both the absolute value and the anisotropic variation of κ is essential for reliable modeling of heat transfer, prevention of

localized overheating, and improvement of the long-term performance of nuclear fuel cladding. In metals and alloys, the κ typically results from both electron (κ_e) and phonon contributions (κ_{ph}) [21]. Although κ_e typically plays a more significant role, both components are critical for the overall thermal management of the cladding. The importance of κ_{ph} lies in two factors: firstly, κ_{ph} is more susceptible to defects caused by irradiation due to its strong dependence on the lattice structure, and secondly, κ_{ph} can be modified and enhanced more easily than κ_e, making it essential for developing materials with high thermal conductivity[22]. Defects caused by irradiation serve as barriers to thermal carriers (electrons, phonons, etc.), thereby reducing κ [23]. Calculating κ, especially for irradiated alloys, is complex and requires an understanding of the interactions between carriers and defects, as well as the influence of various factors. Furthermore, interpreting experimental results is challenging due to the varying contributions of these defects [24, 25]. Simulations provide a more accessible, cost-effective, and safer alternative.

Molecular dynamics (MD) simulations are a suitable method for calculating κ_{ph}, utilizing both equilibrium MD (EMD) and non-equilibrium MD (NEMD) approaches. NEMD methods, which are based on Fourier's law, calculate κ_{ph} by measuring heat flux and temperature gradients [24]. In contrast, EMD methods rely on the Green-Kubo relationship [25]. MD has a rich history of application in the study of κ_{ph} in alloys and metals, with early works focusing on simpler materials and later expanding to more complex systems [18, 23-38]. Although various molecular dynamics methods have been compared for different materials and interatomic potentials [25, 27, 28], the results are highly dependent on the material's structure, potential type, and thermodynamic conditions. In this study, we conducted a comparative analysis specifically tailored to the Zr-1%Nb binary alloy at the operating temperature of VVER (Vodo-Vodyanoi Energeticheskiy Reaktor) reactor fuel cladding, employing two versions of the Angular Dependent Potential (ADP)[39, 40]. The key novelty of this work lies in applying the selected method to investigate the influence of defect distribution on the alloy's thermal conductivity, offering new insights into defect-driven thermal transport behavior in nuclear materials. By focusing on the real-world nuclear alloy Zr-1%Nb, the study's findings are practically relevant for optimizing nuclear materials for safer and more efficient reactor operations.

After evaluating the methods, this work utilizing the Müller-Plathe method to investigate the effects of point defects such

as vacancies, interstitials, and Frenkel pairs on the κ_{ph} of a Zr-1%Nb. The Large-scale Atomic/Molecular Massively Parallel Simulator (LAMMPS)[41] software and the ADP model, which is a generalization of the Emabedded Atom Method (EAM) potential, were used for simulations. The ADP model includes dipole and quadrupole distortions of the local atomic environment and accurately predicts the mechanical properties of Zr-1%Nb [8, 39, 40].

The structure of the article is as follows: First, the methods mentioned for calculating κ_{ph} are described, and the important parameters of each method are introduced, explaining why they need to be optimized. Then, the κ_{ph} of the perfect alloy is calculated by each method using the optimized parameters, and the results are evaluated. After selecting the optimal method and potential, the effects of point defects on κ_{ph} are examined in the subsequent sections, and finally, the results are discussed.

2. Methodology

2.1 Müller-Plathe method

The Müller-Plathe method is one of the NEMD approaches implemented in LAMMPS. The basis of this method is Fourier's law, which calculates κ_{ph} using the temperature gradient, ∇T and heat flux, $\mathbf{J_x}$ [24].

$$\boldsymbol{\kappa_x} = -\frac{\mathbf{J_x}}{\nabla \mathbf{T}} \quad \textbf{(1)}$$

Molecular dynamics simulations do not account for electrons and consequently ignore κ_e. Therefore, the κ calculated using this method represents only the κ_{ph}, in all the three methods considered in this work, the phonon contribution is only calculated.

In NEMD methods for calculating κ_{ph}, a temperature gradient is applied to the system, and the resulting heat flux is measured. However, in the Müller-Plathe method, the process is reversed. The simulation box is divided into $\boldsymbol{n}$ thin layers with the same thickness and perpendicular to the heat flux direction. Then, two layers are considered as hot and cold layers. The hottest atom in the cold layer and the coldest atom in the hot layer are identified, and their energies are exchanged. This exchange occurs at a certain frequency throughout the entire simulation. Ultimately, the exchange of these velocities generates a heat flux, which leads to the establishment of a temperature gradient, as illustrated in Fig.**1**.

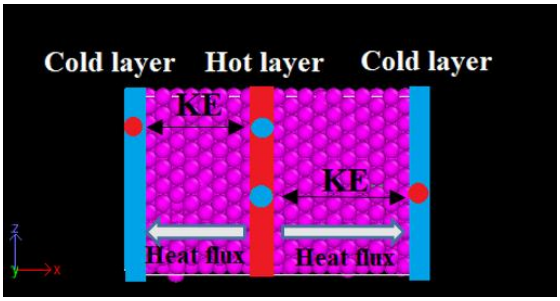


Fig. 1. Schematic of the simulation box layering in the Müller-Plathe method.

In this method, the temperature gradient is not imposed externally but is instead determined by the applied heat flux. This approach converges more quickly because the temperature gradient—the key variable of interest—reaches equilibrium faster. The accelerated convergence arises from the Müller-Plathe method's design, where heat is exchanged between specific regions of the system, ensuring controlled and consistent heat flow. By directly managing energy transfers, this technique reduces statistical noise and produces a smoother, more accurate temperature gradient that better reflects the system's true thermal behavior. The heat flux itself is calculated by summing all the exchanged energies[24].

$$J_x = \frac{\bar{\varepsilon}}{2AWt_{MD}} \quad (2)$$

Where $\bar{\varepsilon}$ is the average energy exchanged, t_{MD} is the simulation time step, W is the energy exchange step, and A is the area of the surface perpendicular to the flux. The factor of 2 indicates that the heat flux flows in two directions. Using just one side of the simulation box can cause asymmetric temperature gradients and boundary effects, distorting the calculations of κ_{ph}. Dividing the simulation box into multiple layers in two directions ensures an even heat flux distribution, leading to more accurate and reliable κ_{ph} measurements.

After the hot and cold layers are created by the heat flux, the temperature gradient is calculated using the temperatures of the hot and cold layers and the length of the simulation box along the heat flux, according to the following equation:

$$\nabla T = \frac{T_{hot} - T_{cold}}{\frac{L_x}{2}} \quad (3)$$

This equation is valid strictly under a linear temperature profile condition. T_{hot} is the temperature of the hot layer, T_{cold} is the temperature of the cold layer, and L_x is the length of the simulation box in the direction of heat flux.

In this method, the parameter W is critical and must be optimized to avoid significant changes and inaccuracies in thermal conductivity. If W is too low, the system doesn't equilibrate properly, leading to non-linear temperature gradients, artificially high heat flux, and overestimated thermal conductivity. Conversely, if W is too high, the heat flux is minimal, resulting in small temperature gradient, high statistical noise, and underestimated thermal conductivity.

To optimize W, it's crucial to maintain a linear temperature profile and steady heat flux for accurate κ_{ph} calculations. Fourier's law assumes these conditions:

- **Linear temperature gradient:** Ensures uniform heat flow and accurate conductivity values.
- **Steady heat flux:** Ensures consistent energy transfer throughout the system.

Deviation from these conditions can lead to significant inaccuracies in the calculated thermal conductivity. The optimization of $\boldsymbol{W}$ parameters was performed in a specific simulation box size and direction. This same value was then applied to other sizes and directions to ensure that the anisotropy in κ_{ph} and differences for various sizes were not due to variations in this parameter.

Non-equilibrium methods calculate κ_{ph} in a single direction for each simulation. In these methods, because the mean free path of the phonons is comparable to the dimensions of the box, the finite size effect is created, and κ_{ph} depends on the length of the simulation box. To neutralize this effect, κ_{ph} should be calculated for different lengths of the simulation box and then extrapolated from the graph relating the inverse of κ_{ph} to the inverse of the simulation box length [26].

2.2 Direct thermostat method

Similar to the previous method, this approach is based on Fourier's law. The simulation box is divided into n layers of equal thickness, perpendicular to the direction of κ_{ph} calculation. Two layers are designated as 'hot' and 'cold' regions, with thermostats maintaining the desired temperatures [42]. See Fig. **2**.

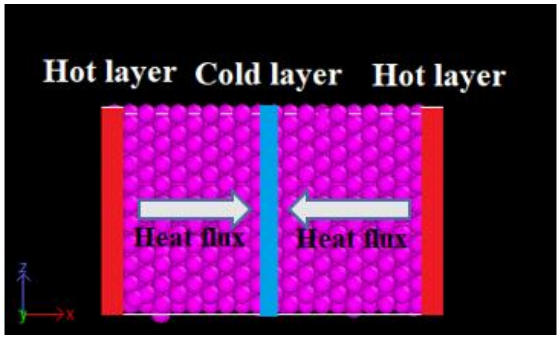


Fig. 2. Schematic of the simulation box layering in the direct thermostat method.

The heat flux is calculated from the average heat flux out of the hot layer and into the cold layer, as shown in Equ. 4:

$$\boldsymbol{J_x = \frac{1}{2}(J_{in} + J_{out})} \quad \textbf{(4)}$$

where $\boldsymbol{J_{out}}$ represents the heat flux exiting the hot layer, and $\boldsymbol{J_{in}}$ represents the heat flux entering the cold layer. The temperature gradient is obtained using the same method as before. The key difference between this method and the previous one lies in how heat flux is generated. In this approach, similar to experimental setups, a temperature gradient is directly imposed, which then drives heat flow. In contrast, the previous method (Müller-Plathe) generates heat flux indirectly by exchanging particle velocities between regions, creating an effective temperature gradient [42].

In this approach, large statistical fluctuations in heat flux require long simulation times for stability. Low

temperature gradients make it difficult to obtain reliable measurements, requiring higher gradients, which can lead to nonlinear temperature profiles and artificial effects, such as boundary heating. These issues may result in inaccuracies in the thermal transport properties.

The temperature gradient applied in this method is crucial and must be chosen optimally. If the temperature gradient is not optimized, significant errors in the calculated thermal conductivity may occur. A large temperature difference can lead to nonlinear heat conduction, causing local phase or structural changes, distorted temperature profiles, and either overestimation or underestimation of thermal conductivity. Conversely, a small temperature difference results in low heat flux, which can yield noise-dominated results and an underestimation of κ_{ph} due to measurement inaccuracies.

To optimize the temperature gradient in the direct thermostat method, it is essential to ensure a linear temperature profile and steady heat flux for accurate calculations of κ_{ph} [42].

2.3 EMD: Green-Kubo method

In this method, the system is in equilibrium (no temperature gradient), and κ_{ph} is calculated using the Green-Kubo formula. This approach relies on the fluctuation-dissipation theorem and linear response theory, utilizing the Heat Current Autocorrelation Function (HCACF) [43]. The κ_{ph} is determined by the decay time of the HCACF. The Green-Kubo formula for κ_{ph} is given by:

$$\boldsymbol{K_x = \frac{1}{VK_BT^2}\int_0^{\tau} \langle J_x(t)\cdot J_x(0)\rangle dt} \qquad \textbf{(5)}$$

where $\boldsymbol{K_x}$ is the x-component of thermal conductivity, $\boldsymbol{V}$ is the volume of the system, $\boldsymbol{K_B}$ is the Boltzmann constant, $\boldsymbol{T}$ is the temperature $\langle \boldsymbol{J_x(t)\cdot J_x(0)}\rangle$ is the HCACF, $\boldsymbol{J_x}$ refers to the x-component of the heat flux and $\boldsymbol{\tau}$ represents the correlation time required for the HCACF to decay sufficiently.

To compute this in a molecular dynamics simulation, the continuous integral is approximated by a discrete sum. The continuous time variable $\boldsymbol{t}$ is replaced with discrete time steps $\boldsymbol{n\Delta t}$. The integral is then approximated by a sum over these discrete time steps [43]:

$$\boldsymbol{K_x = \frac{\Delta t}{VK_BT^2}\sum_{m=1}^{M}\frac{1}{N-m}\sum_{n=1}^{N-m} J_x\big((m+n)\Delta t\big)J_x(n\Delta t)} \qquad \textbf{(6)}$$

Where $\boldsymbol{N}$ is the total number of time steps, $\boldsymbol{M}$ is the correlation length that determines the range over which the autocorrelation function is calculated, and $\boldsymbol{\Delta t}$ is the time interval between each data sampling point.

The heat flux is defined as the time derivative of the sum of the products of the site energies and the positions of the particles:

$$\boldsymbol{J = \frac{d}{dt}\sum_i r_i(t)\varepsilon_i(t)} \quad \textbf{(7)}$$

where $\boldsymbol{r_i}$ is the time-dependent position of atoms and $\boldsymbol{\varepsilon_i}$ is the site energy, which is the sum of the kinetic and potential energies of the $\boldsymbol{i}$-th atom:

$$\boldsymbol{\varepsilon_i = \frac{1}{2}m_i v_i^2 + \frac{1}{2}\sum_j u_2(r_{ij}) + \frac{1}{6}\sum_{jk} u_3(\mathbf{r}_i, \mathbf{r}_j, \mathbf{r}_k)} \quad \textbf{(8)}$$

where $\mathbf{v_i}$ is the velocity of atom *i,* and $\boldsymbol{u_2}$ and $\boldsymbol{u_3}$ represent two-body and three-body potentials, respectively. The corresponding heat current can then be calculated using the following expression:

$$\mathbf{J}(t) = \sum_i \mathbf{v}_i\varepsilon_i + \frac{1}{2}\sum_{ij} \mathbf{r}_{ij}(\mathbf{F}_{ij}\cdot\mathbf{v}_i) + \frac{1}{6}\sum_{ijk} (\mathbf{r}_{ij} + \mathbf{r}_{ik}) \times (\mathbf{F}_{ijk}\cdot\mathbf{v}_i) \quad \textbf{(9)}$$

where $\mathbf{r_{ij}} = \mathbf{r_i} - \mathbf{r_j}$, and $\mathbf{F_{ij}}$ and $\mathbf{F_{ijk}}$ represent two-body and three-body forces.

For the Green-Kubo relation to accurately calculate thermal conductivity, the correlation integral must converge. If the normalized HCACF converges to a non-zero value, the heat will tend to infinity, resulting in unrealistic and infinite heat values. In physical systems, after some time, molecular motions and heat flows reach a random state, indicating that the system has reached thermal equilibrium. If the correlation function converges to a non-zero value, it suggests that heat flow still partially depends on its initial state, which is inconsistent with physical reality.

The damping requirement of the correlation function involves optimizing the sampling interval and correlation length. Sparse sampling can miss important fluctuations, leading to inaccurate results, while overly frequent sampling introduces noise. The correlation length is the time over which the HCACF is integrated to obtain κ_{ph} and should be optimized to ensure convergence. If the correlation length is too short, the integral might not converge, leading to underestimation of the thermal conductivity. Conversely, if it's too long, unnecessary data could introduce noise, since the correlation between heat current at distant times diminishes (i.e., it becomes essentially zero). To optimize these parameters, the decay of HCACFs is first analyzed, and correlation lengths are calculated for various sample intervals and potentials. Then, by examining the temporal and spatial convergence of thermal conductivity, the appropriate potential and values are determined.

Due to the random distribution of alloy particles and defects in the simulation box,

multiple samples are needed to achieve accurate and representative results in both EMD and NEMD methods. However, EMD methods typically require fewer samples compared to NEMD, as EMD computes κ in three directions within each simulation. This method integrates the heat current autocorrelation function over time, and the results are less sensitive to the size of the simulation box because it averages over many phonon wavelengths. Therefore, EMD typically exhibits a smaller size effect compared to NEMD. Despite these advantages, the EMD method requires more computation time due to the complexity of calculating heat flux. The three-body potential contributions are often neglected to facilitate calculations, leading to reduced accuracy, especially for irradiated alloys where the three-body potential plays a significant role.

2.4 Data files generation with ATOMSK

The first step to simulate κ_{ph} is to model the perfect and defective Zr-1% Nb alloy. The Zr–1%Nb single crystal studied here serves as an idealized model for the Russian E110 polycrystalline alloy used in nuclear fuel cladding. The base component of this alloy is zirconium, with the following elemental composition (in wt%): Nb (0.9–1.1), Fe (0.015), Ni (0.007), Al (0.004), Ti (0.003), C (0.02), Si (0.004), O (0.05), N (0.003), and H (0.001–0.002) [44].While the actual E110 alloy contains trace impurities and polycrystalline structure [45], these were omitted in our MD simulations due to computational constraints and limitations of the employed interatomic potential. To model Zr–1%Nb single crystal, zirconium super-cells of varying sizes and orientations were first created using ATOMSK [46], (with lattice parameters a=b=3.213 Å, c=5.164 Å) [39]. For two non-equilibrium methods, super-cells with sizes of 8*6* (30, 40, 50 and 60) were created in the following directions. Periodic boundary conditions were applied in x, y, and z along the $[\bar{1}2\bar{1}0]$, $[10\bar{1}0]$ and $[0001]$directions respectively. One atomic percent of the zirconium atoms were then randomly replaced with niobium to create Zr-1% Nb super-cells. Based on the investigation type, different samples with varying niobium distribution in the alloy were prepared. Equilibrium simulation boxes were also created in the same manner as the non-equilibrium method, using the sizes indicated in the results. To create vacancy defects, a certain percentage of zirconium atoms in the complete structure were randomly removed. For interstitial defects, a certain percentage of zirconium atoms was added to the structure. To create Frenkel pair defects, a specific percentage was removed while an additional percentage was added. These randomly dispersed defects are introduced with an

inter-defect distance of at least 1.5 times the lattice parameter to minimize the likelihood of defect recombination or clustering. Four defect concentrations were considered in this work: 0.5%, 1%, 1.5%, and 2%. Fig. **3** shows a schematic representation of the production of 1% of different defects. To cover different defect distributions, various samples were made for each density.

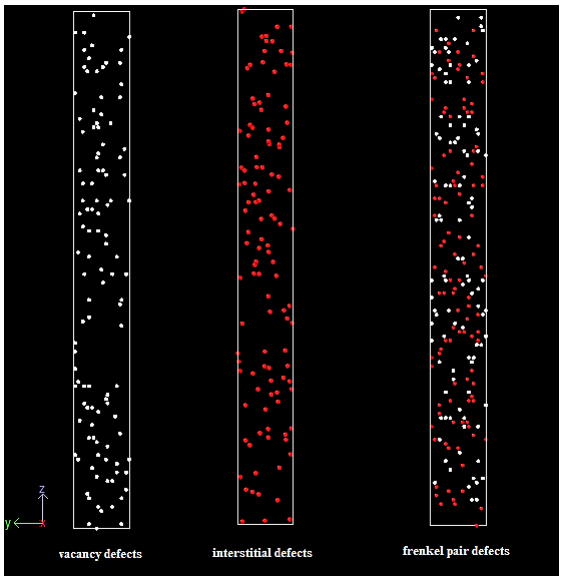


Fig. 3. In a super cell with 8×6×60 cells (11520 atoms), typical samples of each type of point defect were included at a concentration of 1%**.**

To ensure the validity of the potential version used, we first calculate several thermal properties before determining the thermal conductivity. These properties include the isobar heat capacity using equation (10), and the volume expansion coefficient, calculated using equation (11). The calculations are performed for the perfect structure with the size of 10×10×10 unit cells.

$$\boldsymbol{c_p = \left(\frac{\partial H}{\partial T}\right)_p} \quad \textbf{(10)}$$

$$\boldsymbol{\beta = \frac{1}{V_0}\frac{\partial V}{\partial T}} \quad \textbf{(11)}$$

where $\boldsymbol{H}$ represents enthalpy, $\boldsymbol{V}$ is volume, $\boldsymbol{P}$ is pressure, and $\boldsymbol{T}$ stands for temperature. The electronic contribution to the heat capacity has been neglected. To calculate the average phonon thermal conductivity, the κ_{ph} was calculated in three directions x, y and z along the $[\bar{1}2\bar{1}0]$, $[10\bar{1}0]$ and $[0001]$ directions, respectively. To calculate κ_{ph} in each direction, super-cells were created by copying the appropriate unit cell. For instance, to calculate conductivity along the $x = [\bar{1}2\bar{1}0]$ orientation, the simulation box sizes were 30×8×6, 40×8×6, 50×8×6 and 60×8×6 cells. The same approach was used for the y and z directions. Finally, the average phonon thermal conductivity (κ_{ph}) was calculated using the following relation

$$\boldsymbol{\kappa_{ph} = \frac{\kappa_x + \kappa_y + \kappa_z}{3}} \quad \textbf{(12)}$$

2.5 LAMMPS parameters details

To evaluate the ADP potential version, the perfect structure created by ATOMSK in the previous step was first relaxed and then minimized. The NPT ensemble was then applied at temperature ranging from 200 to 1000 K, with a temperature step of 100 K

and a target pressure of 1 atmosphere for 1 ns.

To calculate the κ_{ph} of both the perfect and defective structure using two non-equilibrium methods, the created structures were first relaxed and minimized. The NVT ensemble was applied initially to equilibrate the system for 0.5 ns, targeting a temperature of 600 K, which is representative of the operating temperature of nuclear fuel cladding in reactors [47]. Following this, the NVE ensemble was applied, and the κ_{ph} was calculated using the Müller-Plathe method. The time step for all the simulation processes was set to 2 fs, with a total simulation time of 1.5 ns (7.5×10^5 MD steps). For the equilibrium method, the time step was set to 1 femtosecond, with an equilibrium time of 0.5 nanoseconds in the NVT ensemble. The κ_{ph} was calculated in the NVE ensemble over a period of 3 nanoseconds.

3. Results and discussion

3.1 The evaluation of potentials

The simulation results of the evaluation of two different versions of the ADP potential are presented in Fig. **4** and Fig. **5**. The results indicate both versions encounter challenges to accurately predict thermal expansion and specific heat capacity, though the 2017 version performs relatively better. This is likely because the ADP 2021 potential focuses on accurately describing crystal phases and defects in the Zr-Nb system. This emphasis on phase stability and defect properties likely led to parameter adjustments that reduced its precision in capturing atomic vibrations and dynamic behaviors essential for accurate thermal property predictions.

The bends or inflection points in the curves of Figs. 4 and 5 can be attributed to limitations or transitions in the atomic-scale behavior captured by the ADP potentials (2017 and 2021). Here's a breakdown for each: in Fig. 4 experimental curve is smooth and increases steadily, as expected for Zr. ADP-2021 shows a significant bend around 600 K, after which β starts decreasing.

Possible reasons:

Potential artifact: The ADP-2021 may not accurately model anharmonic effects or thermal expansion at higher temperatures. Lattice instability: The potential might cause non-physical stiffening or softening in atomic vibrations beyond a certain temperature. Phase-related effects: While no actual phase transition occurs in this range for Zr, the potential might mimic a pseudo-transition (e.g., change in dominant vibration modes or bonding behavior). In Fig. 5 experimental Cp increases linearly, consistent with Dulong-Petit law at higher T and increased phonon contributions. ADP-2021 again shows a bend/drop around 600 K, deviating from linear behavior. Likely reasons:

Phonon anharmonicity misrepresentation: Cp should increase with T due to anharmonic effects, but the 2021 potential may underestimate them.

Mismatch in vibrational DOS: The potential could inaccurately shift vibrational modes or suppress soft modes.

Parameter fitting limit: The ADP-2021 might be fitted only up to a certain temperature range, causing deviations beyond it.

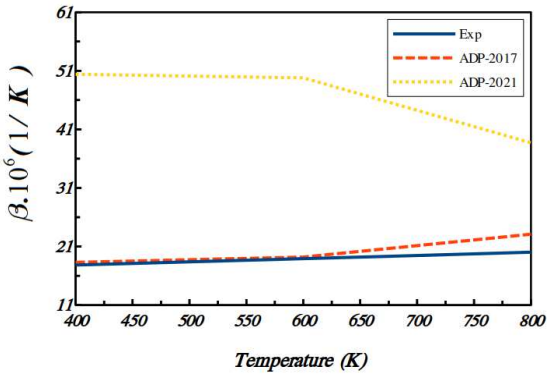


Fig. 4. Volume expansion coefficient versus temperature for two different versions of ADP potential and experimental values of reference [44].

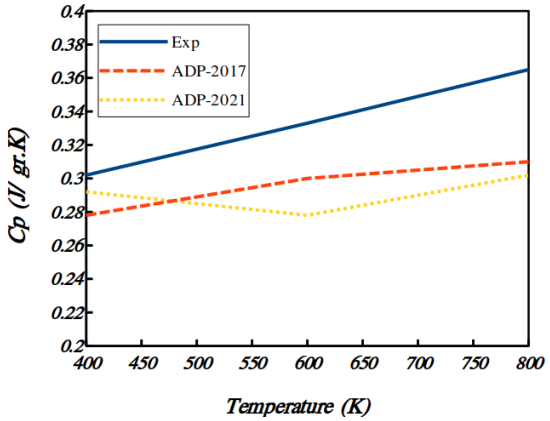


Fig. 5. Isobar heat capacity versus temperature for two different versions of ADP potential and experimental values of reference [44].

These observations raise a fundamental question: if a potential fails to accurately describe basic thermal properties such as Cp and β, can its predictions for phonon thermal conductivity (κ_{ph}) be considered reliable? This concern is entirely valid, as all these properties originate from the same underlying vibrational physics. However, the simultaneous presentation and analysis of κ_{ph} results from both ADP potentials in this study is justified by the following considerations:

First, it is important to distinguish between absolute quantitative accuracy and qualitative comparative analysis. While ADP-2021 clearly under performs in reproducing experimental benchmarks for β and C_p, presenting its κ_{ph} results alongside those of ADP-2017 serves a valuable comparative purpose. This side-by-side comparison allows us to examine how the deficiencies in capturing anharmonic behavior (evidenced by the poor β predictions) propagate into the thermal conductivity calculations. Does the anomalous behavior observed around 600 K in Fig. 4 and Fig. 5 manifest similarly in κ_{ph}? If so, this would confirm a direct link between the misrepresentation of anharmonicity and errors in transport properties. If not, it might suggest a degree of error cancellation or differing sensitivities of these properties to specific aspects of the interatomic potential.

Second, the comparison provides insight into the trade-offs inherent in potential development. The ADP-2021 potential was developed with a focus on phase stability and defect structures properties that are critical for many materials science applications but do not necessarily correlate strongly with accurate thermal transport predictions. The contrast between its performance for structural properties (presumably improved) and thermal properties (demonstrably worse) highlights the importance of selecting potentials based on the specific target properties of interest. For studies focused exclusively on thermal transport, the ADP-2017 version appears more suitable, whereas for studies requiring accurate defect physics, ADP-2021 might still be preferred despite its thermal limitations.

Third, we emphasize that the inclusion of ADP-2021 results in our analysis is not intended to imply equal validity or quantitative accuracy of its κ_{ph} predictions. Rather, these results are presented in the spirit of scientific transparency to provide a complete picture of the current capabilities and limitations of available potentials for the Zr-Nb system. By explicitly documenting where and why ADP-2021 fails (as evidenced by the deviations in Fig. 4 and Fig. 5), we offer clear guidance to other researchers who might consider using these potentials for similar studies.

It should also be noted that in the high-temperature regime relevant to many engineering applications, the specific heat capacity approaches the classical Dulong-Petit limit. Under such conditions, even a potential with inaccuracies in the fine details of the phonon density of states may yield C_p values close to the correct limit, potentially mitigating the impact of these errors on κ_{ph} calculations. However, the persistent errors in thermal expansion a direct indicator of anharmonicity remain a significant concern and suggest that the κ_{ph} results from ADP-2021, particularly their temperature dependence, should be interpreted with considerable caution.

In summary, while we acknowledge the limitations of the ADP-2021 potential for thermal property predictions, its inclusion alongside ADP-2017 provides a valuable comparative perspective. This approach highlights the sensitivity of thermal transport calculations to potential parameterization and underscores the critical importance of validating interatomic potentials against a comprehensive suite of thermal properties including both harmonic (C_p) and anharmonic (β) indicators before employing them for predictive studies of heat conduction.

3.2 The optimizing the parameters of each method

The simulation results for optimizing W of the Müller-Plathe method are presented in Fig. **6**, **7**, **8**, and **9**.

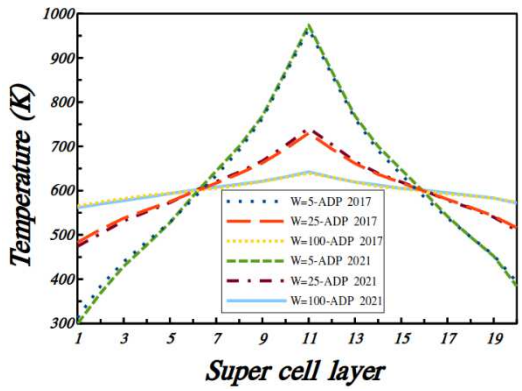


Fig. **6**. Temperature profile of the simulation box with dimensions 8×6×30 in the [0001] direction, considerin two potential versions and three values of W in the Müller-Plathe method.

Fig. **6** illustrates the temperature profiles for various W values, including two ADP potential versions. The simulation box dimensions are 8×6×30 with 20 layers, oriented in the [0001] direction, and the temperature is set at 600 K for a consistent alloy sample. The results indicate that, regardless of the potential version, higher W values cause the graph to deviate from linearity. Conversely, while smaller W values produce a linear graph, the temperature gradient is very small. The difference in the potential versions does not significantly affect the temperature profile.

Fig. **7** also presents the steady results of the heat flux for the same simulation setup as Fig. **6** The heat flux remains steady for all W values, and the impact of the potential version is negligible.

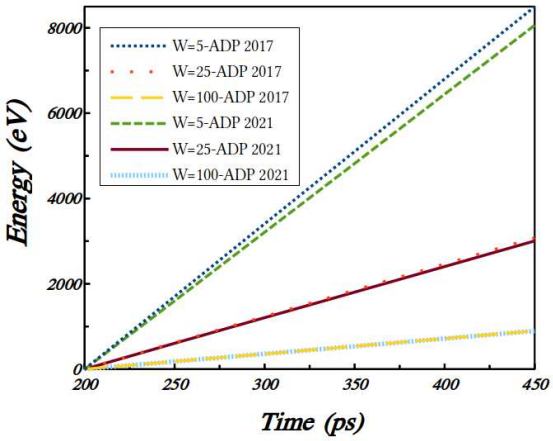


Fig. **7**. Exchanged energy over time for a simulation box with dimensions 8×6×30 in the [0001] direction, considering two potential versions and three values of W in the Müller-Plathe method.

The results from Fig. **6** and **7** show that W=25 is an optimal and suitable value in the Müller-Plathe method. This value satisfies both the linearity of the temperature profile and the steadiness of the heat flux.

Fig. **8** shows the temperature profile versus the length of the simulation box along the heat flux direction for different layer configurations, all with W=25. It indicates that varying the number of layers (N) has little effect on the slope and linearity of the temperature profile. Fig. **9** further demonstrates that the heat flux remains consistent across all layer configurations.

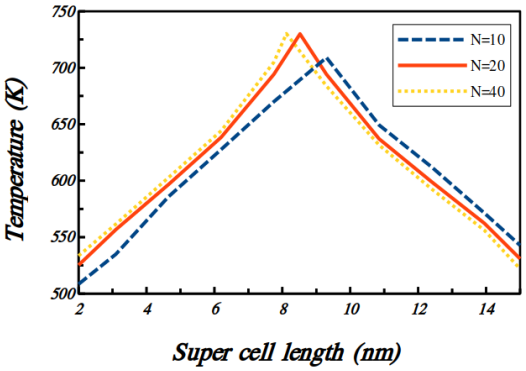


Fig. 8. Temperature vs. Super-cell Length along the Heat Flux Direction for Different Layer Counts in the Müller-Plathe Method.

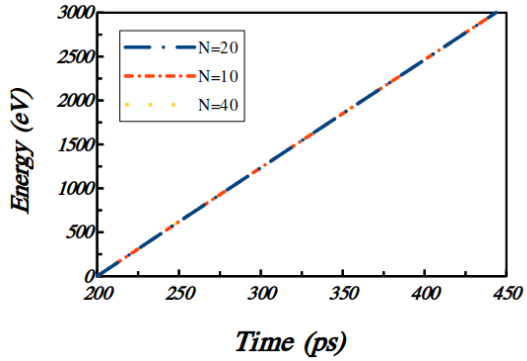


Fig. 9. Exchanged energy over time for Different Layer Counts in the Müller-Plathe Method.

The number of layers in the simulation box may not significantly affect the calculated thermal conductivity. This is because the method relies on energy exchange between specific regions within the simulation. Energy is directly exchanged between two designated layers, so even if the number of layers changes, the energy exchange remains efficient and consistent, leading to reliable κ calculations. This method minimizes the influence of boundary effects and the number of layers, ensuring uniform heat distribution throughout the simulation. Consequently, κ is primarily dependent on parameters such as W and potential type, rather than the number of layers.

Fig. **10** and **11** present the simulation results for optimizing the temperature gradient parameter, which is a crucial factor in the direct thermostat method.

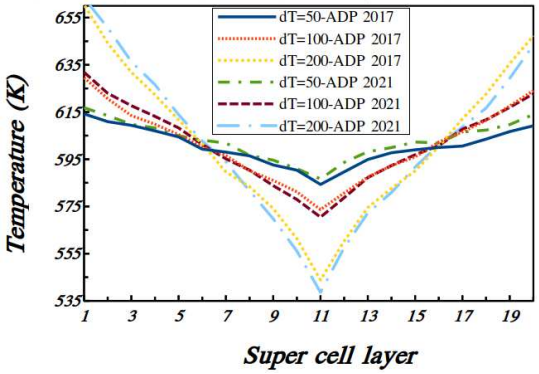


Fig. 10. Temperature profile of the simulation box with dimensions 8×6×30 in the [0001] direction, considering two potential versions and three values of temperature gradient in the direct thermostat method.

Fig. **10** demonstrates the temperature profiles for various temperature gradients including two ADP potential versions. The simulation box dimensions are 8×6×30 with 20 layers, oriented in the [0001] direction. The temperature is set at 600 K, and this analysis is conducted on a consistent alloy sample.

The dT=50 Shows a very steep gradient. Temperature drop is too sharp and non-linear near the center. dT=200 Still shows noticeable non-linearity in the middle layers. Slight improvement over dT=50, but the gradient is not smooth or symmetric. dT=100 Produces the smoothest and most symmetric temperature profile. The gradient looks more linear and stable, especially in the center region. This is true for both the ADP 2017 and 2021 potentials.

Fig. **11** shows the heat flux exiting the hot layer and entering the cold layer for dT=100

and two potential versions. The results indicate that the heat flux is in a steady state. Based on this figure and the previous one, dT=100 appears to be an optimal value for the direct thermostat method.

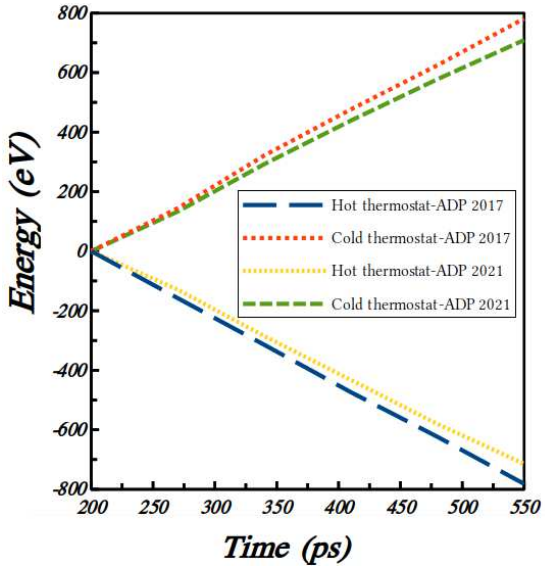


Fig. **11**. Energy exiting the hot layer and energy entering the cold layer over time for a simulation box with dimensions 8×6×30 in the [0001] direction, considering two potential versions in direct thermostat method.

Fig. **12** and **13** present the simulation results for optimizing the sample interval and correlation length parameters in the Green-Kubo method.

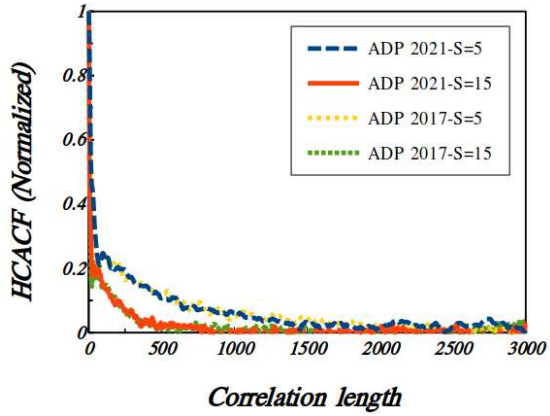


Fig. **12**. Normalized HCACF as a function of Correlation Length for different Sample Intervals and two versions of the potential in Green-Kubo method.

Fig. **12** shows the decay of the normalized HCACF for two different sample intervals and two versions of the potential. The alloy sample remains consistent across all tests, and the box size is 10×10×10. The results indicate that smaller sample interval reveals finer temporal details in the heat current, capturing longer-lasting correlations in the system. This leads to a longer correlation length in the HCACF because the autocorrelation function decays more slowly when measured with high time resolution.

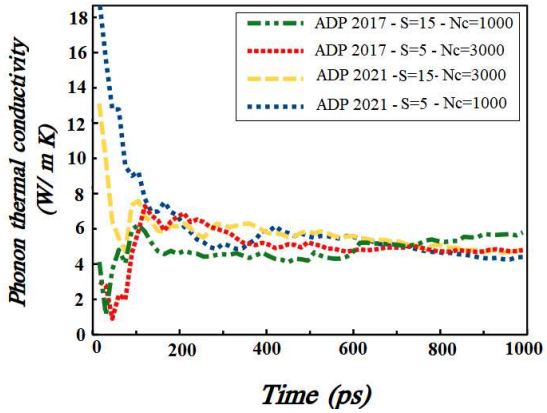


Fig. **13**. κ_{ph} over time for different Sample Intervals and correlation lengths for two versions of the potential in Green-Kubo method.

Fig. **13** represents the average κ_{ph} over time for three alloy samples, different sample intervals, and correlation lengths, using two versions of the potential in the Green-Kubo method. These results indicate that κ_{ph} for the 2017 potential version, with a smaller sample interval but a larger correlation length, exhibits better decay. This is because smaller sample intervals capture more detailed and continuous data, enhancing the accuracy of κ_{ph}

measurements. However, larger correlation lengths provide a better representation of long-term interactions and energy transfer, leading to more stable and realistic results over time.

3.3 κ_{ph} of Perfect Zr-1%Nb

Fig. **14**. illustrates the simulation results of κ_{ph} using the Müller-Plathe method. The results are shown for two potential versions, across three crystallographic directions, and for four sizes. Temperature is set at 600 K, and w is 25. For each size, the κ_{ph} is averaged over three alloy samples.

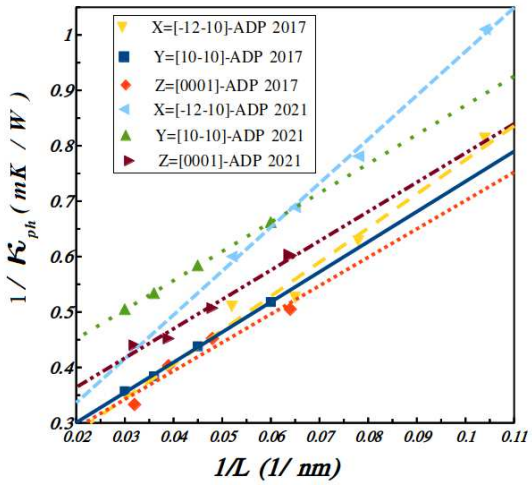


Fig. 14. Inverse of κ_{ph} of perfect Zr-1%Nb versus the inverse of the simulation box length along the heat flux in three directions, using two potentials in the Müller-Plathe method.

The calculated results from graphs are given in Table 1.

Table 1

κ_{ph} of perfect Zr-1%Nb at 600 K for different crystallographic orientation in the Müller-Plathe method.

Direction	K_i (W/ mK)	
	ADP 2017	ADP 2021
$[\bar{1}2\bar{1}0]$	4.47	3.2
$[10\bar{1}0]$	4.21	2.82
[0001]	3.87	2.42

Fig. **15** shows the same simulation setup for the direct thermostat method. The results are displayed under the same conditions for consistency. Instead of w=25, which specific to the Müller-Plathe method, ΔT=100K is used.

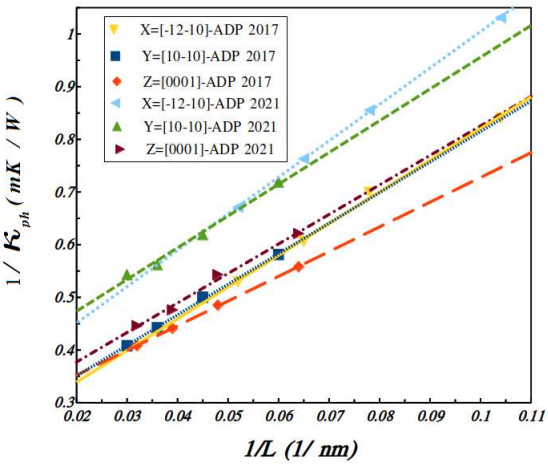


Fig. 15. Inverse of κ_{ph} of perfect Zr-1%Nb versus the inverse of the simulation box length along the heat flux in three directions, using two potentials in the direct thermostat method.

The calculated results from graphs are given in Table 2.

Table 2

κ_{ph} of perfect Zr-1%Nb at 600 K for different crystallographic orientation in the direct thermostat method.

Direction	K_i (W/ mK)	
	ADP 2017	ADP 2021
$[\bar{1}2\bar{1}0]$	6.28	5.64
$[10\bar{1}0]$	5.23	2.9
[0001]	5.31	3.87

Both methods show that the κ_{ph} along $[\bar{1}2\bar{1}0]$is greater than in the other two directions. This is due to the higher atomic density in this direction. Additionally, the κ_{ph} obtained with the 2017 ADP potential version is larger compared to the 2021 ADP version. Considering that thermal conductivity

in solids is heavily influenced by phonon scattering mechanisms, this shows that the ADP 2021 potential might predict stronger phonon scattering and capture anharmonicity, leading to lower thermal conductivity values.

Fig. **16** demonstrates the simulation results for the decay of the normalized HCACF. It covers different sizes with a sample interval of 5, a correlation length of 3000, and the ADP 2017 potential in the Green-Kubo method. The same alloy sample is used. For sizes larger than 5×5×5, the HCACF shows consistent decay behavior. For smaller sizes, significant fluctuations occur.

These severe fluctuations in the HCACF for smaller systems are primarily due to finite size effects, boundary impacts, and insufficient averaging over a larger number of particles or longer distances. These factors, combined with stronger thermal or statistical noise and a lack of self-averaging behavior, lead to more pronounced irregularities in the HCACF compared to larger systems, where these effects are smoothed out.

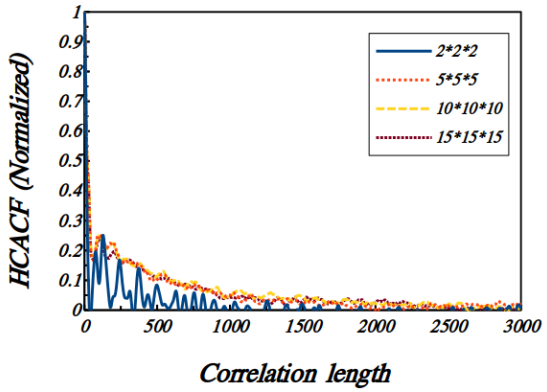


Fig. 16. Normalized HCACF as a function of Correlation Length for different super-cell **sizes** in Green-Kubo method.

Fig. **17** presents the decay of κ_{ph} for different sizes using a sample interval of 5 and a correlation length is 3000, based on the 2017 potential. The results are averaged over three alloy samples for each size. The data indicates that for sizes larger than 5, the convergence of κ_{ph} across different sizes becomes similar, due to a weaker size effect. Additionally, the optimized sample interval and correlation length for a size of 10×10×10 can serve as a good starting point; however, it is essential to re-optimize these parameters for different system sizes, especially if the system is significantly larger or smaller than the one used in the initial optimization.

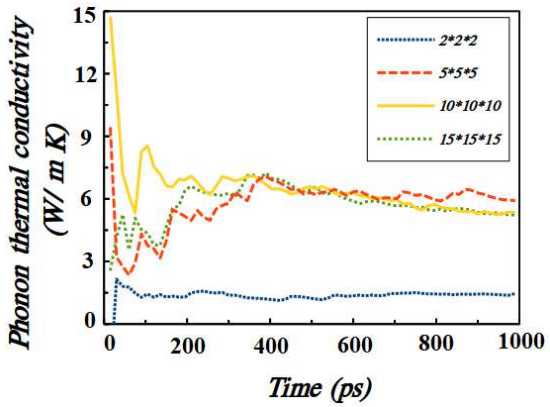


Fig. 17. κ_{ph} over time for different super-cell sizes in Green-Kubo method.

In conclusion, Table **3** presents the κ_{ph} results obtained from three methods, across two potential versions, using the optimized parameters for each method.

Table 3

κ_{ph} of perfect Zr-1%Nb at 600 K from three methods for two version ADP potential.

Method	K_{ph} (W/ mK)	
	ADP 2017	ADP 2021
Müller-Plathe	4.18	2.89
Direct thermostat	5.6	4.13
Green-Kubo	5.76	5.5

The κ_{ph} of the Zr-1%Nb alloy is around 3-4 W/mK at 600 K [44]. Based on this, the Müller-Plathe method for both potential versions, as well as the direct thermostat method for the 2021 potential version, provide acceptable results for phonon thermal conductivity. Although tuning simulation parameters can lead to improvements, the major discrepancy in κ_{ph} usually arises from the accuracy of the interatomic potential. To reduce this gap, it is essential to focus on selecting and validating an appropriate potential.

3.4 Thermal Modeling Impact on Nuclear Fuel Safety

The heat generated by nuclear fission is transferred to the coolant through a sequence of three to four thermal resistance steps: conduction through the fuel pellet, conduction (or thermal contact) across the fuel–cladding gap, conduction through the cladding, and finally convection to the coolant. This process can be expressed by the following steady-state relation [48]:

$$T_{cf} - T_{fl} = \frac{q}{2\pi r_f}\left[\frac{r_f}{2\kappa_f} + \frac{1}{h_G} + \frac{t_c}{(\kappa_{ph}+\kappa_e)_c} + \frac{r_f}{h_s(r_f+t_c)}\right] \quad (13)$$

where T_{cf} is the fuel centerline temperature, T_{fl} is the coolant temperature, q is the linear heat generation rate, r_f is the fuel pellet radius, κ_f is the fuel thermal conductivity, h_G is the effective fuel–cladding gap conductance, is the t_c cladding thickness, κ_{ph} and κ_e are the phonon and electronic components of cladding thermal conductivity, and h_s is the coolant surface heat transfer coefficient. As seen from the above equation, there is a strong incentive to maximize all heat transfer coefficients in order to increase the allowable linear heat rate and reduce the risk of fuel melting. For safe operation, the

fuel centerline temperature must remain below the fuel melting point (≈2800 °C for UO_2). However, during the reactor operating cycle, thermal conductivities tend to degrade due to irradiation damage, oxidation, crud deposition, and pellet restructuring, while the effective melting margin may also decrease with burnup. Reactor design must therefore ensure that remains safely below the critical melting limit throughout the fuel lifetime.

In this work, the centerline temperature was calculated for different values of obtained from various MD methods and interatomic potentials. If the differences between models were large, the choice of model could have a noticeable impact on , and therefore on optimized and safe reactor design. In such cases, it would be prudent to adopt the most conservative (lowest conductivity) model to preserve safety margins.

The results presented in Table 4 , however, indicate that the variation in obtained from different MD approaches and different versions of the ADP potential leads to negligible differences in predicted fuel centerline temperature under nominal steady-state reactor operating conditions.

Table 4
Centerline fuel temperature associated with different thermal conductivity methods

Method	T_{cf} (°C)	
	ADP 2017	**ADP 2021**
Müller-Plathe	761.95	761.97
Direct thermostat	761.92	761.95
Green-Kubo	761.92	761.93

The computed values differ by less than 0.05 °C between the lowest and highest conductivity cases. This difference is several orders of magnitude smaller than the total centerline temperature rise, which is typically in the range of several hundred degrees Celsius for LWR fuel rods. The small sensitivity can be attributed to the fact that, in the thermal resistance chain from fuel centerline to coolant, the cladding conduction term, contributes only a very small fraction to the total temperature drop. The dominant contributions arise from fuel pellet conduction and fuel–cladding gap resistance, followed by the coolant film coefficient. As a result, variations in within the range considered here have an insignificant effect on the total between coolant and fuel centerline.

From a design and safety evaluation standpoint, this finding implies that for nominal steady-state operation, the uncertainty in from MD potential or methodology selection does not measurably affect thermal margins. Fuel melt limits (~2800 °C for UO_2) and cladding temperature limits (~700–900 °C for high-burnup Zr alloys) remain unaffected. Consequently, while accurate thermal

conductivity models are essential for detailed materials characterization and transient modeling, under steady-state nominal conditions the uncertainty in can be considered secondary to other operational uncertainties. Safety evaluations should thus prioritize the accurate characterization of gap conductance degradation, oxide/crud layer formation, and coolant thermal–hydraulic conditions, which dominate the thermal margin.

Finally, these findings provide important context for the translation of atomistic-scale MD results to engineering-scale thermal models. While MD simulations are invaluable for understanding the microscopic origins of thermal transport and for parameterizing high-fidelity material property databases, not all property variations have equal significance in full-scale reactor performance predictions. In this case, MD-predicted differences in are real and scientifically relevant, but their engineering impact on steady-state fuel rod thermal limits is minimal. This highlights the need for careful filtering of atomistic-level outputs to identify which material property variations are critical to incorporate into fuel performance codes such as BISON or FRAPCON, particularly for design-basis safety evaluations.

3.5 Anisotropy of κ_{ph} reduction

In this section, the results related to the effects of point defects on the κ_{ph} using the Müller-Plathe method and the ADP 2017 potential are presented. The results (Fig. 18) show that for all defect types, the κ_{ph} decreases with increasing defect concentration in all directions. This trend is expected, as higher defect concentrations enhance phonon-defect scattering, reduce the phonon mean free path, and consequently lower κ_{ph}. Order of κ_{ph} Reduction: Vacancy > Frenkel Pair > Interstitial. This order can be explained by the degree of lattice disruption caused by each defect type: Vacancies create missing atoms in the lattice, which strongly disrupt periodicity and act as potent scattering centers for phonons, leading to a significant reduction in κ_{ph}. Frenkel pairs, consisting of a vacancy and an interstitial, cause considerable lattice distortion, but the presence of the displaced atom partially maintains vibrational continuity, resulting in a less severe reduction than vacancies alone. Interstitials add extra atoms at non-lattice sites, introducing localized strain. However, the overall scattering effect is milder compared to vacancies and Frenkel pairs, especially because interstitials tend to adopt stable configurations.

The reduction in κ_{ph} is not uniform across crystallographic directions, indicating that

defect type and configuration interact with the anisotropic phonon transport of the HCP Zr lattice.

Vacancies: The largest reduction in κ_{ph} occurs in the $x = [\bar{1}2\bar{1}0]$ direction, with nearly equal reductions in the $y = [10\bar{1}0]$ and $z = [0001]$ directions. This directional preference likely arises from anisotropic phonon velocities and the defect scattering cross-section being higher along $x = [\bar{1}2\bar{1}0]$ where phonons are more efficiently disrupted by vacancies.

Interstitials: The anisotropy is most pronounced for interstitials, with the largest κ_{ph} reduction along $x = [\bar{1}2\bar{1}0]$ and the smallest along $y = [10\bar{1}0]$. This behavior correlates with findings from various studies that show interstitial defects in Zr preferentially stabilize in the Basal Octahedral (BO) configuration[49-51]. The BO site lies within or near the basal planes and offers energetic stability, especially along the $y = [10\bar{1}0]$ direction. Interstitials in these stable configurations cause less disruption to phonon transport, resulting in reduced scattering and a smaller decline in κ_{ph} in that direction.

Frenkel pairs:

The greatest reduction is observed in the $z = [0001]$ direction. This may be attributed to the complex interaction between the vacancy and interstitial components, which can disrupt the c-axis more significantly.

Summary of Findings (up to 2% defect concentration):

- Order of κ_{ph} reduction: Vacancy > Frenkel pair > Interstitial
- Anisotropy in κ_{ph} reduction behavior: Interstitial > Frenkel pair > Vacancy
- $[10\bar{1}0]$ direction consistently shows the smallest reduction for all three defect types.
- Order of κ_{ph} reduction for interstitial defects: $[\bar{1}2\bar{1}0] > [0001] > [10\bar{1}0]$
- Order of κ_{ph} reduction for vacancy defects: $[\bar{1}2\bar{1}0] > [0001] > [10\bar{1}0]$
- Order of κ_{ph} reduction for Frenkel pair defects: $[0001] > [\bar{1}2\bar{1}0] > [10\bar{1}0]$

The summary of results is presented in Table 4.

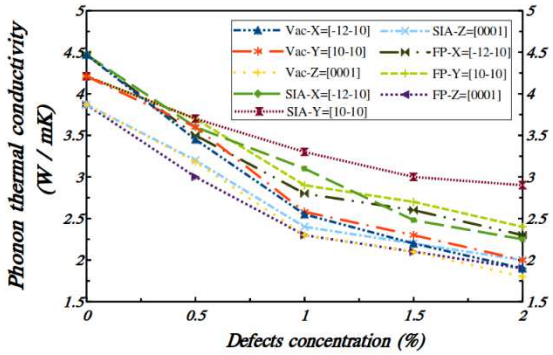


Fig. 18. κ_{ph} versus defects concentration at 600 K and in different orientation in Müller-Plathe method.

Table 4
Percentage reduction of κ_{ph} in different directions for different defects

	$[\bar{1}2\bar{1}0]$	$[10\bar{1}0]$	[0001]	Average
Vac	57%	52%	53%	54%
SIA	50%	31%	48%	43%
FP	48%	44%	50%	47%

4. Conclusion

In this work, we first evaluated three molecular dynamics methods for calculating the κ_{ph} of the Zr-1%Nb alloy: the equilibrium method (EMD), the non-equilibrium direct thermostat method, and the Müller-Plathe method. This comparison was conducted at 600 K for two ADP versions of the potential, using the optimal parameters for each method.

The results indicate that EMD methods are less affected by size effects, requiring a smaller simulation box with fewer samples of alloy particles and defects. However, they necessitate a longer time for the decay of the heat current autocorrelation function (HCACF). Additionally, they take more time to calculate complex heat flux for the complex potential of irradiated alloys. Consequently, the three-body potential term is often overlooked, which is crucial for irradiated alloys and reduces the accuracy of the method. Therefore, we turned to the NEMD method.

Between NEMD methods, the direct thermostat method requires a large temperature gradient to achieve accurate heat flux measurements. However, this high temperature gradient can introduce several issues, such as nonlinear temperature profiles and enhanced boundary effects, which can distort the results. Consequently, the Müller-Plathe method is preferred as it allows for a more controlled and accurate measurement of κ_{ph} without the need for such a large temperature gradient.

Both the 2017 and 2021 versions of the ADP potential produce acceptable κ_{ph} values close to experimental data, with the 2021 potential consistently yielding lower values across all methods compared to the 2017 potential. However, both versions struggle to accurately predict other thermal properties, such as thermal expansion and specific heat capacity, though the 2017 version performs relatively better. The 2021 version exhibits greater deviations from experimental thermal property data, therefore, the thermal conductivity results derived from it are less reliable. The results also indicate that the centerline temperature differences corresponding to various κ_{ph} calculation methods are less than 0.05°C. This negligible variation confirms that uncertainties in phonon-based conductivity modeling have no meaningful impact on fuel thermal performance under steady-state conditions.

In the second section, we used the Müller-Plathe method to examine the effects of various point defects on thermal conductivity. The results demonstrate that vacancy defects have a greater impact on reducing thermal conductivity. Additionally, the reduction in κ_{ph} varies anisotropically with different defects, reflecting the anisotropic distribution of the defects and varying degrees of strain and

phonon scattering caused by different types of defects in different crystallographic directions.

Funding: The authors declare that no funds, grants, or other support were received during the preparation of this manuscript.

References

[1] R.A. Razak, A. Afzal, A.M. Samee, M. Ramis, Effect of cladding on thermal behavior of nuclear fuel element with non-uniform heat generation, Progress in Nuclear Energy 111 (2019) 1-14.https://doi.org/10.1016/j.pnucene.2018.10.013

[2] D.O. Northwood, The development and applications of zirconium alloys, Materials & design 6(2) (1985) 58-70.https://doi.org/10.1016/0261-3069(85)90165-7

[3] H.G. Rickover, L.D. Geiger, B. Lustman, History of the development of zirconium alloys for use in nuclear reactors, Energy Research and Development Administration, Washington, DC (USA). Div …, 1975,

[4] A. Savchenko, A. Vatulin, A. Morozov, G. Kulakov, S. Ershov, A. Laushkin, S. Maranchak, Y. Konovalov, E. Malamanova, Zirconium alloys matrix as innovative material for composite fuel, Progress in Nuclear Energy 57 (2012) 138-144.https://doi.org/10.1016/j.pnucene.2011.10.016

[5] S.S. Mustafa, The possibility of utilizing novel cladding materials instead of zirconium in light water reactors, Nuclear Engineering and Design 431 (2025) 113733

[6] F. Kerze, B. Lustman, The metallurgy of zirconium, McGraw-Hill1955.

[7] B. Bell, S. Murphy, P. Burr, R. Comstock, J. Partezana, R. Grimes, M. Wenman, The influence of alloying elements on the corrosion of Zr alloys, Corrosion Science 105 (2016) 36-43.https://doi.org/10.1016/j.corsci.2015.12.022

[8] M. Basaadat, M. Payami, S. Sheykhi, Analysis of Irradiation Induced Defect Clusterization for Zr-1% Nb Alloy Using Atomistic Simulation, Journal of Nuclear Research and Applications 3(2) (2023) 15-21.https://doi.org/10.24200/jon.2023.0621

[9] I. Chant, K. Murty, Structural materials issues for the next generation fission reactors, Jom 62 (2010) 67-74.http://dx.doi.org/10.1007/s11837-010-0142-3

[10] P. Yvon, F. Carré, Structural materials challenges for advanced reactor systems, Journal of nuclear materials 385(2) (2009) 217-222.http://dx.doi.org/10.1016/j.jnucmat.2008.11.026

[11] C.R.d.F. Azevedo, A review on neutron-irradiation-induced hardening of metallic components, Engineering Failure Analysis 18(8) (2011) 1921-1942.http://dx.doi.org/10.1016/j.engfailanal.2011.06.008

[12] T.S. Byun, K. Farrell, M. Li, Deformation in metals after low-temperature irradiation: Part II–Irradiation hardening, strain hardening, and stress ratios, Acta Materialia 56(5) (2008) 1056-1064.http://dx.doi.org/10.1016/j.actamat.2007.10.056

[13] M. Fregonese, C. Régnard, L. Rouillon, T. Magnin, F. Lefebvre, C. Lemaignan, Failure Mechanisms of irradiated Zr alloys related to PCI: Activated slip systems, localized strains, and iodine-induced stress corrosion cracking, Zirconium in the Nuclear Industry: Twelfth International Symposium, ASTM International, 2000,

[14] S. Mohamed, G. Po, R. Lewis, P. Nithiarasu, Multiscale computational study to predict the irradiation-induced change in engineering properties of fusion reactor materials, Nuclear materials and energy 39 (2024) 101647.https://doi.org/10.1016/j.nme.2024.101647

[15] F. Onimus, S. Doriot, J.-L. Béchade, Radiation effects in zirconium alloys, Comprehensive Nuclear Materials 3 (2020) 1-56.http://dx.doi.org/10.1016/B978-0-12-803581-8.11759-X

[16] Y. Deng, B. Qiu, B. Pang, X. Gong, Y. Wu, G. Su, X. Huang, Y. Li, Y. Yin, Research on performance enhancement of nuclear fuel with SiC cladding by using high thermal conductivity fuels, Progress in Nuclear Energy 124 (2020) 103330.https://doi.org/10.1016/j.pnucene.2020.103330

[17] K.F. Lunn, D. Apelian, Thermal and Electrical Conductivity of Aluminum Alloys: fundamentals, structure-property relationships, and pathways to enhance conductivity, Materials Science and Engineering: A (2024) 147766.https://doi.org/10.1016/j.msea.2024.147766

[18] Y. Mao, Y. Li, Y. Xiong, W. Xiao, Point defect effects on the thermal conductivity of β-SiC by molecular dynamics simulations, Computational Materials Science 152 (2018) 300-307.http://dx.doi.org/10.1016/j.commatsci.2018.05.050

[19] M.O. Yilmaz, M.N. Avramova, J.G. Andersen, Impact of fuel thermal conductivity degradation on Doppler feedback during rod ejection accident, Nuclear Engineering and Design 307 (2016) 339-353

[20] A. Toptan, R.K. Salko, M.N. Avramova, K. Clarno, D.J. Kropaczek, A new fuel modeling capability, CTFFuel, with a case study on the fuel thermal conductivity degradation, Nuclear Engineering and Design 341 (2019) 248-258

[21] O. Kahveci, E. Çadirli, M. Arı, H. Tecer, M. Gündüz, Measurement and prediction of the thermal and electrical conductivity of Al-Zr overhead line conductors at elevated temperatures, Materials Research 22(1) (2018) e20180513.http://dx.doi.org/10.1590/1980-5373-mr-2018-0513

[22] Z. Tong, S. Li, X. Ruan, H. Bao, Comprehensive first-principles analysis of phonon thermal conductivity and electron-phonon coupling in different metals, Physical review B 100(14) (2019) 144306.https://doi.org/10.1103/PhysRevB.100.144306

[23] Z. Wang, C. Yang, M. Yu, W. Ma, L. Guo, Z. Wei, N. Gao, Z. Yao, X. Wang, Dependence of thermal conductivity on radiation defects in ThO2 investigated by molecular dynamics method, Nuclear Materials and Energy (2024) 101673.https://doi.org/10.1016/j.nme.2024.101673

[24] F. Müller-Plathe, A simple nonequilibrium molecular dynamics method for calculating the thermal conductivity, The Journal of chemical physics 106(14) (1997) 6082-6085.https://doi.org/10.1063/1.473271

[25] P.K. Schelling, S.R. Phillpot, P. Keblinski, Comparison of atomic-level simulation methods for computing thermal conductivity, Physical Review B

65(14) (2002) 144306.https://doi.org/10.1016/j.molliq.2021.117478
[26] Y. Mao, D. Hu, C. Wu, Q. Liu, Y. Xiong, Vacancy defects effect on thermal conductivity of α-zirconium crystal, Materials Research Express 6(11) (2019) 116531.https://doi.org/10.1088/2053-1591/ab4314
[27] J. Ryu, T. Oda, H. Tanigawa, Comparison and validation of the lattice thermal conductivity formulas used in equilibrium molecular dynamics simulations for binary systems, Computational Materials Science 178 (2020) 109615.https://doi.org/10.1016/j.commatsci.2020.109615
[28] A. Soleimani, H. Araghi, Z. Zabihi, A. Alibakhshi, A comparative study of molecular dynamics simulation methods for evaluation of the thermal conductivity and phonon transport in Si nanowires, Computational Materials Science 142 (2018) 346-354.https://doi.org/10.1016/j.commatsci.2017.10.024
[29] B. Fu, W. Lai, Y. Yuan, H. Xu, W. Liu, Calculation and analysis of lattice thermal conductivity in tungsten by molecular dynamics, Journal of nuclear materials 427(1-3) (2012) 268-273.https://doi.org/10.1016/j.jnucmat.2012.05.015
[30] A.V. Lunev, B.A. Tarasov, A classical molecular dynamics study of the correlation between the Bredig transition and thermal conductivity of stoichiometric uranium dioxide, Journal of nuclear materials 415(2) (2011) 217-221.https://doi.org/10.1016/j.jnucmat.2011.06.009
[31] S. Nichenko, D. Staicu, Molecular Dynamics study of the mixed oxide fuel thermal conductivity, Journal of nuclear materials 439(1-3) (2013) 93-98.https://doi.org/10.1016/j.jnucmat.2013.03.075
[32] G. Samolyuk, S. Golubov, Y. Osetsky, R. Stoller, Molecular dynamics study of influence of vacancy types defects on thermal conductivity of β-SiC, Journal of Nuclear Materials 418(1-3) (2011) 174-181.https://doi.org/10.1016/j.jnucmat.2011.06.036
[33] T. Uchida, T. Arima, K. Idemitsu, Y. Inagaki, Thermal conductivity of non-stoichiometric americium oxide: A molecular dynamics study, Journal of nuclear materials 400(1) (2010) 3-7.https://doi.org/10.1016/j.jnucmat.2010.02.001
[34] X.-G. Liang, B. Shi, Two-dimensional molecular dynamics simulation of the thermal conductance of superlattices, Materials Science and Engineering: A 292(2) (2000) 198-202.https://doi.org/10.1016/S0921-5093(00)01012-1
[35] M. Rajabi, M. Hassanvand, M.A. Asadabad, M. Amirkhani, Molecular dynamics simulation of phonon thermal conductivity variation in E110 alloy post operation in VVER-type reactor irradiation conditions, Journal of Nuclear Materials (2025) 155872.https://doi.org/10.1016/j.jnucmat.2025.155872
[36] D. Guo, H. Gong, M. Chen, Y. Chen, S. Wang, J. Zhai, X. Zhang, Y. Yan, Z. Lu, J. Wang, Computational framework for thermal conductivity and volumetric swelling of irradiated silicon carbide, Nuclear Engineering and Design 438 (2025) 114073
[37] C.I. Maxwell, J. Pencer, Molecular dynamics modelling of the thermal conductivity of off-stoichiometric UO2±x and (UyPu1− y) O2±x using equilibrium molecular dynamics, Annals of Nuclear Energy 131 (2019) 317-324.https://doi.org/10.1016/j.anucene.2019.03.029
[38] Q. Wang, N. Gui, Y. Luo, X. Yang, J. Tu, S. Jiang, Effect of metal fission products on the thermal transport of SiC/PyC nanocomposites: Insight from molecular dynamics simulations, Annals of Nuclear Energy 226 (2026) 111849.https://doi.org/10.1016/j.anucene.2025.111849
[39] D. Smirnova, S. Starikov, Study of niobium diffusion and clusterization in hcp zr-nb dilute alloys, Defect and Diffusion Forum, Trans Tech Publ, 2017, pp. 167-174
[40] S. Starikov, D. Smirnova, Optimized interatomic potential for atomistic simulation of Zr-Nb alloy, Computational Materials Science 197 (2021) 110581.https://doi.org/10.1016/j.commatsci.2021.110581
[41] A.P. Thompson, H.M. Aktulga, R. Berger, D.S. Bolintineanu, W.M. Brown, P.S. Crozier, P.J. In't Veld, A. Kohlmeyer, S.G. Moore, T.D. Nguyen, LAMMPS-a flexible simulation tool for particle-based materials modeling at the atomic, meso, and continuum scales, Computer physics communications 271 (2022) 108171.https://doi.org/10.1016/j.cpc.2021.108171
[42] P. Howell, Thermal conductivity calculation with the molecular dynamics direct method I: more robust simulations of solid materials, Journal of Computational and Theoretical Nanoscience 8(10) (2011) 2129-2143.https://doi.org/10.1166/jctn.2011.1935
[43] A.I. Khan, I.A. Navid, M. Noshin, H.A. Uddin, F.F. Hossain, S. Subrina, Equilibrium molecular dynamics (MD) simulation study of thermal conductivity of graphene nanoribbon: a comparative study on MD potentials, Electronics 4(4) (2015) 1109-1124.https://doi.org/10.3390/electronics4041109
[44] V. Bobkov, L. Fokin, E. Petrov, V. Popov, V. Rumiantsev, A. Savvatimsky, Thermophysical properties of materials for nuclear engineering: a tutorial and collection of data, IAEA, Vienna (2008) 18-21
[45] Y.P. Sharkeev, A.Y. Eroshenko, S. Fortuna, A. Tolmachev, T. Fink, STRUCTURE AND MECHANICAL PROPERTIES OF ULTRA-GRAINED ZIRCONIUM ALLOYED WITH NIOBIUM UNDER SEVERE PLASTIC DEFORMATION, Izvestiya. Ferrous Metallurgy 56(8) (2015) 60-64
[46] P. Hirel, Atomsk: A tool for manipulating and converting atomic data files, Computer Physics Communications 197 (2015) 212-219.https://doi.org/10.1016/j.cpc.2015.07.012
[47] S. Pelykh, M. Maksimov, V. Baskakov, Grounds of VVER-1000 fuel cladding life control, Annals of Nuclear Energy 58 (2013) 188-197.https://doi.org/10.1016/j.anucene.2013.03.020
[48] J.J. Duderstadt, L.J. Hamilton, Nuclear reactor analysis, Wiley1976.
[49] M. Christensen, W. Wolf, C. Freeman, E. Wimmer, R. Adamson, L. Hallstadius, P. Cantonwine, E. Mader, Diffusion of point defects, nucleation of dislocation loops, and effect of hydrogen in hcp-Zr: Ab initio and classical simulations, Journal of Nuclear Materials 460 (2015) 82-96.https://doi.org/10.1016/j.jnucmat.2015.02.013
[50] Y.N. Osetsky, D. Bacon, N. De Diego, Anisotropy of point defect diffusion in alpha-zirconium, Metallurgical and Materials Transactions A 33 (2002) 777-782.DOI: 10.1007/s11661-002-0144-z
[51] M. Zhou, B. Fu, Q. Hou, L. Wu, R. Pan, Determining the diffusion behavior of point defects in zirconium by a multiscale modelling approach, Journal of Nuclear Materials 566 (2022) 153772.https://doi.org/10.1016/j.jnucmat.2022.153772